CHEMISTRY OF MATERIALS
Cite This: Chem. Mater. 2019, 31, 90−100
Article
pubs.acs.org/cm

Atomic Layer Deposited TiO_2−IrO_x Alloys Enable Corrosion Resistant Water Oxidation on Silicon at High Photovoltage

Olivia L. Hendricks,[†] Robert Tang-Kong,[‡] Aein S. Babadi,[‡] Paul C. McIntyre,[*,‡] and Christopher E. D. Chidsey[*,†]

[†]Department of Chemistry, Stanford University, Stanford, California 94305, United States
[‡]Department of Materials Science and Engineering, Stanford University, Stanford, California 94305, United States

Supporting Information

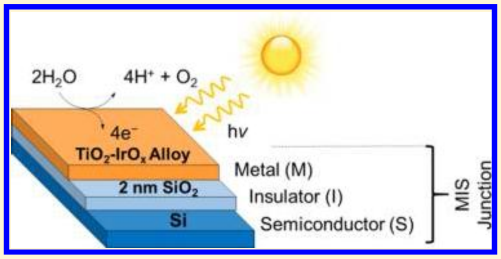

ABSTRACT: We synthesized by atomic layer deposition (ALD) TiO_2−IrO_x alloys that enable high photovoltages and catalyze water oxidation on silicon metal−insulator−semiconductor (MIS) photoanodes. The ratio of TiO_2 to IrO_x was precisely controlled by varying the number of ALD cycles for each precursor. Silicon with a 2 nm surface SiO_2 layer was coated with TiO_2−IrO_x alloys ranging in composition from 18 to 35% iridium relative to the sum of titanium and iridium concentrations. IrO_x catalyzed oxygen evolution and imparted a high work function to the TiO_2−IrO_x alloys, enabling photovoltages during water oxidation that exceeded 600 mV. TiO_2 imparted stability and inhibited corrosion of the underlying silicon light absorber. After annealing in forming gas (5% H_2/95% N_2), TiO_2−IrO_x alloys were stable for 12 h of continuous water oxidation in 1 M H_2SO_4. Key properties of the MIS junction affecting electrochemical operation were also extracted by electrochemical impedance spectroscopy. This work demonstrates that alloying by ALD is a promising approach for designing corrosion resistant Schottky contacts with optimized electronic and materials properties for catalyzed, solar driven water oxidation.

INTRODUCTION

Any efficient photoanode for solar-driven water oxidation requires (1) a high yield of energetic photogenerated carriers, (2) a mechanism for extracting these carriers at high photovoltage, (3) an effective catalyst for water oxidation, and (4) corrosion resistance at the pH, potential and illumination conditions used in device operation. Metal−insulator−semiconductor (MIS) photoanodes are capable of generating large photovoltages,[1−6] but preventing corrosion of the underlying semiconductor during water oxidation remains a challenge. We previously demonstrated that atomic layer deposited TiO_2−RuO_2 alloys (the “M” of the MIS photoanode) achieved photovoltages of 500 mV on *n*-type silicon; however, RuO_2 was lost from the oxide within minutes when exposed to the electrolyte during photoanode operation.[7] As a result, we replaced ruthenium with iridium, which is thermodynamically more stable under the conditions required for water oxidation. In this work, we demonstrate that TiO_2−IrO_x alloys can generate photovoltages above 600 mV, catalyze water oxidation, and prevent corrosion of the underlying silicon during 12 h of continuous operation in acid.

In an MIS photoanode, the metal induces a built-in field at the semiconductor/insulator interface that extracts photogenerated carriers from the semiconductor absorber. The Schottky barrier associated with this field dictates the photovoltage of the device. It depends on the difference between the metal and semiconductor work functions, taking fixed charges and surface states into account.[4,8] For an *n*-type semiconductor photoanode, a high work function metal induces a field that sweeps photogenerated holes to the electrolyte interface for water oxidation. If the metal work function is sufficiently close to the valence band edge of the *n*-type semiconductor, it generates an inversion layer at the semiconductor/insulator interface.[1,4,9−11] The result is a MIS junction that matches the performance of a *p*−*n* diode.[4,9,12]

Using an MIS junction to drive water oxidation in a photoelectrochemical cell, however, introduces several new engineering challenges. In addition to generating large photovoltages, the ideal Schottky contact must also catalyze oxygen evolution and protect the underlying semiconductor from corrosion. Transition metal oxides like CoO_x, NiO_x, and FeO_x have been used as catalysts and Schottky contacts to *n*-type silicon photoanodes, but their stability is limited to basic electrolytes.[13−15] Atomic layer deposited TiO_2 has been used to protect silicon in both acid and base,[2,16−18] but it makes a poor Schottky contact to *n*-type silicon.[3]

Alloying TiO_2 with a conductive, high work function, and catalytically active metal oxide is a promising approach for improving the electronic properties of TiO_2. In principle, such alloys combine the corrosion resistance of TiO_2 with the high work function, conductivity, and catalytic activity of the metal oxide. Building on our initial investigation of TiO_2−RuO_2 alloys, we show that TiO_2−IrO_x alloys function as catalytically active Schottky contacts to *n*-type silicon with greatly improved

Received: July 20, 2018
Revised: December 8, 2018
Published: December 10, 2018

DOI: 10.1021/acs.chemmater.8b03092

corrosion resistance in acid. The photoanode structure is shown in Figure 1, in which TiO_2−IrO_x alloys function as the "M" of an MIS junction. TiO_2−IrO_x alloys with 18−35% Ir relative to Ti generated even higher photovoltages than TiO_2−RuO_2 alloys on *n*-type silicon: the maximum recorded photovoltage was 638 mV. We introduce a model for charge transport across the MIS junction based on data from electrochemical impedance Spectroscopy (EIS). The dominant source of low frequency impedance across the junction was the SiO_2 tunnel resistance, which depended strongly on the alloy composition. EIS also provided a measure of the SiO_2 capacitance, and hence the SiO_2 thickness, before and after long-term water oxidation. The SiO_2 capacitance did not change after 12 h of continuous water oxidation in 1 M H_2SO_4, supporting the claim that TiO_2−IrO_x alloys successfully prevent oxidation of the underlying silicon. By investigating the chemical and electronic properties of these alloys, we identified some of the key design principles for corrosion resistant Schottky contacts in MIS photoanodes.

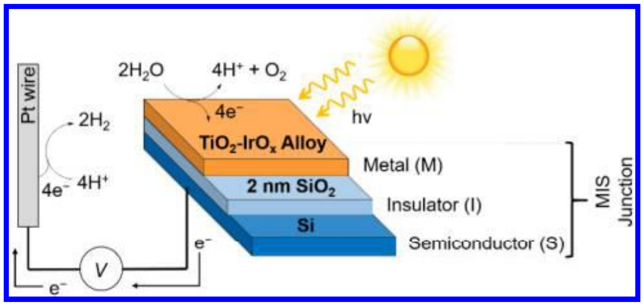

Figure 1. Structure of silicon MIS photoanode coated with TiO_2−IrO_x alloys grown by atomic layer deposition. The SiO_2 thickness is approximately 2 nm as measured by ellipsometry prior to any deposition. The silicon wafer vendor-supplied SiO_2 "chemical oxide" is the substrate for TiO_2−IrO_x alloy ALD for all samples.

Though we use silicon as a model system, the ALD alloying approach is particularly valuable for semiconductors that cannot form high quality p^+n homojunctions. These semiconductors rely on MIS junctions to generate large photovoltages. ALD enables unusually precise control over both the film thickness and composition of the metal layer in an MIS junction. As such, ALD is capable of addressing many of the challenges associated with fabricating carrier-selective contacts in photoelectrochemical and photovoltaic devices.

2. RESULTS AND DISCUSSION

2.1. Characterization of TiO_2−IrO_x Alloys. TiO_2 films were grown by atomic layer deposition (ALD) using tetrakis(dimethylamido)titanium (TDMAT) and water vapor.[19] ALD IrO_x films were grown using 1-ethylcyclopentadienyl-1,3-cyclohexadiene iridium(I) ((EtCp)Ir(CHD)) and ozone.[20,21] TiO_2−IrO_x alloys were grown by an ALD alloying process in which individual cycles of TiO_2 and IrO_x were alternated. The ratio of TiO_2 to IrO_x cycles controlled the Ir content in the film. This cycle ratio was repeated for a designated number of ALD supercycles to control the film thickness. For example, one supercycle of a 1:4 alloy would include one ALD cycle of TiO_2 followed by four ALD cycles of IrO_x. The specific ALD pulse sequence is listed in Table S1.

Figure 2 shows ALD qualification data for IrO_x and TiO_2−IrO_x alloy films. ALD qualification data for TiO_2 was published previously.[7,19] We found that IrO_x films did not initiate well on

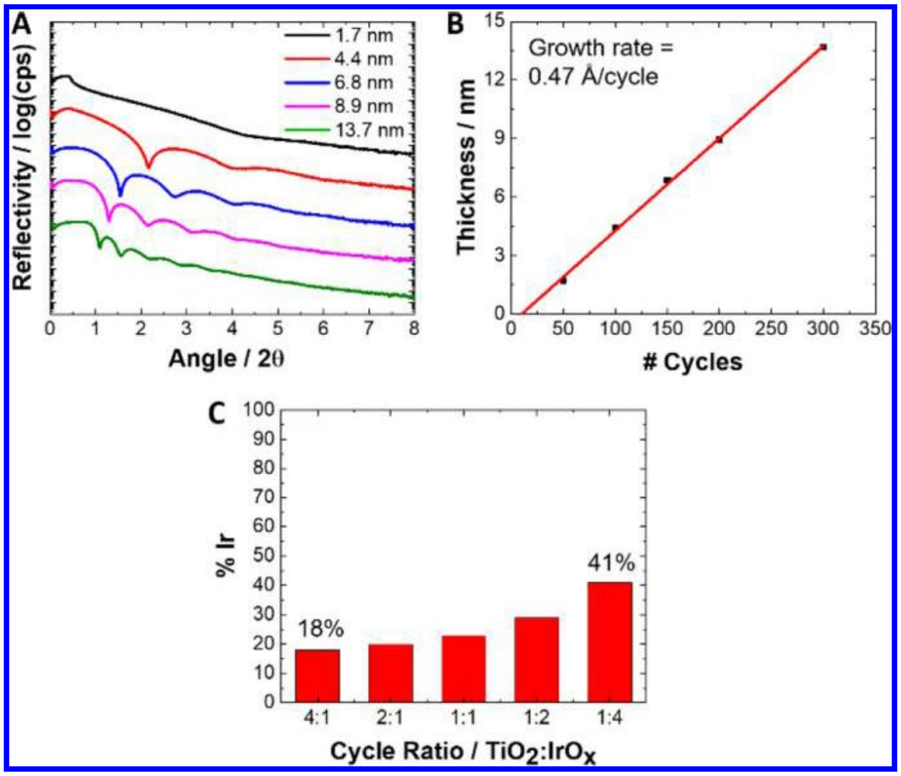

Figure 2. (A) X-ray reflectivity (XRR) data for ALD IrOx films ranging from 1.7 to 13.7 nm. (B) Thickness as determined by XRR as a function of ALD cycles. (C) % Ir concentration relative to the sum of Ti and Ir concentrations as a function of TiO_2:IrO_x cycle ratio. % Ir was calculated from the integrated area under the Ir 4f and Ti 2p peaks in the high resolution X-ray photoelectron spectra (XPS).

DOI: 10.1021/acs.chemmater.8b03092
Chem. Mater. 2019, 31, 90−100

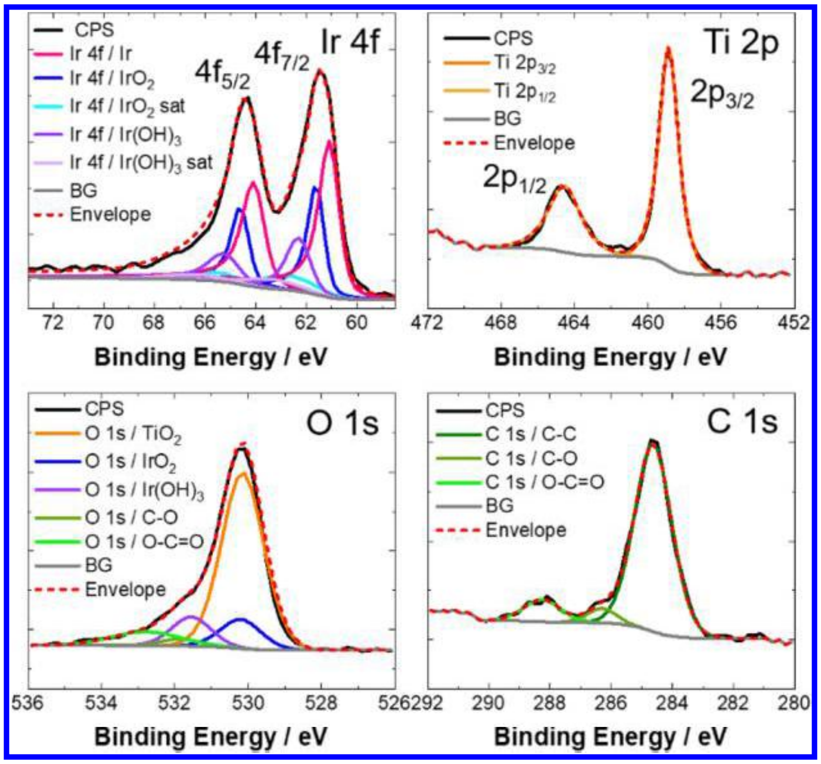

Figure 3. High resolution XPS data for a 7 nm 20% TiO_2−IrO_x alloy after annealing in forming gas at 450 °C for 30 min. No silicon substrate peaks were observed (mean free path for Si 2p electrons is 2.7 nm in TiO_2).

SiO_2, and as a result, 10 cycles of TiO_2 ALD were performed immediately prior to iridium deposition. Film thickness was measured by X-ray reflectivity (XRR), as shown in Figure 2A. Details of the XRR fitting procedure can be found in the Supporting Information, but qualitatively, the decreased period of interference oscillations corresponds to increased film thickness. As shown in Figure 2B, the average growth rate for ALD IrO_x films was 0.47 Å/cycle, similar to previous literature reports at 170 °C.[20]

Figure 2C shows the average composition, determined by X-ray photoelectron spectroscopy (XPS), as a function of cycle ratio for TiO_2−IrO_x alloy films. By varying the ALD cycle ratio, we could control the alloy composition from 14% to 68% Ir. The growth per cycle for TiO_2−IrO_x alloys was consistent with individual growth rates for ALD TiO_2[7,19] and ALD IrO_x.[20] A more detailed discussion of the growth per cycle as a function of alloy composition accompanies Figure S4 in the Supporting Information. Cross-sectional transmission electron microscopy images are also presented in Figure S5. Henceforth, alloys shall be identified by their composition, i.e., a 20% TiO_2−IrO_x alloy is one that contains 20% iridium relative to the sum of iridium and titanium concentrations.

For photoelectrochemical testing, all samples were annealed in forming gas (5% H_2/95% N_2) for 30 min at 450 °C and 1 atm total pressure. As discussed in the Supporting Information, the forming gas anneal densified the films, promoting stability during long-term water oxidation.

After annealing in forming gas, the iridium to oxygen ratio in TiO_2−IrO_x alloy films was determined by XPS. Annealing in forming gas at 450 °C reduced nonalloyed ALD IrO_x to metallic iridium (Figure S9), but the presence of TiO_2 could stabilize a higher oxygen to iridium ratio in TiO_2−IrO_x alloys after annealing. In our previous work, alloying TiO_2 with RuO_2 favored the deposition of RuO_2 instead of metallic ruthenium.[7]

Table 1. Atomic Composition Determined by X-ray Photoelectron Spectroscopy of a 20% ALD TiO_2−IrO_x Alloy Film after Annealing in Forming Gas for 30 min at 450 °C

Atom	Atom%	Binding Energy (eV)
Ir/Ir^0	3.8	61.0 ($4f_{7/2}$)
Ir/$Ir(OH)_3$	1.8	62.3 ($4f_{7/2}$)
Ir/IrO_2	2.7	61.6 ($4f_{7/2}$)
Ti/TiO_2	17.5	458.9 ($2p_{3/2}$)
O/TiO_2	34.1	530.2
O/IrO_2	5.5	530.2
O/$Ir(OH)_3$	5.3	531.6
O/C—O	1.2	531.8
O/O—C=O	4.4	532.8
C/C—C	20.0	284.6
C/C—O	1.2	286.3
C/O—C=O	2.3	288.3

Figure 3 shows high resolution spectra for a 7 nm 20% TiO_2−IrO_x alloy after annealing in forming gas. Table 1 summarizes the composition of the alloy along with relevant binding energies. The iridium 4f region was fit according to previous literature reports, which identify three main iridium species according to the binding energy of the Ir $4f_{7/2}$ component: metallic iridium (Ir^0) at 60.9 eV, IrO_2 (Ir^{IV}) at 61.5−61.8 eV, and IrO_x (Ir^{III}) at 62.3 eV.[22,23] The assignment of a lower iridium oxidation state to a higher binding energy is counterintuitive, but others note similar behavior for silver and cadmium oxides.[24] This Ir^{III} peak assignment has been accepted in several reports, and we will continue to assign this peak to Ir^{III} for consistency.[22,25−27] Further details of the fitting procedure can be found in the Supporting Information.

As shown in Figure 3, the Ir $4f_{7/2}$ component for metallic iridium (pink traces) appeared at 61.0 eV.[22] The Ir $4f_{7/2}$ component for for Ir^{IV} (dark blue traces) appeared at 61.6 eV. Fitting oxidized iridium also required three satellite peaks,[22] which are shown in light blue for Ir^{IV}. The Ir $4f_{7/2}$ component for Ir^{III} (purple traces) appeared at 62.3 eV, and its three satellite peaks are shown in light purple.

The chemical nature of the Ir^{III} peak was determined from the O 1s region. IrO_x thin films are known to acquire a wide range of chemical compositions, and Ir^{III} could originate from Ir_2O_3 or from $Ir(OH)_3$.[28−30] Two O 1s components at 530.2 eV correspond to oxygen from TiO_2 (orange trace) and IrO_2 (blue trace). This binding energy assignment agrees with previous literature reports,[30−32] as well as the binding energy we observed for the O 1s peak of nonalloyed TiO_2[7] and IrO_2 (Figure S8). Oxygen from C—O and O—C═O (green traces) appear at 531.8 and 532.7 eV, respectively.[33] The remaining O 1s component at 531.6 eV (light purple trace) corresponds to the Ir^{III} species. The binding energy of this component suggests hydroxide character,[25,30,34,35] and the area of the peak agrees with an O:Ir^{III} ratio of 1:3. Thus, we attribute the Ir^{III} species to $Ir(OH)_3$. Based on this analysis, the average iridium to oxygen ratio in the annealed 20% TiO_2−IrO_x alloy was approximately 1:1.3, or $IrO_{1.3}$. Combined with the distribution of iridium oxidation states in the Ir 4f region, we conclude that iridium in annealed TiO_2−IrO_x alloys is 46% metallic, 33% IrO_2, and 21% $Ir(OH)_3$. Thus, it appears that alloying ALD IrO_x with TiO_2 indeed stabilizes a higher oxygen to iridium ratio than nonalloyed ALD IrO_x when subjected to the same annealing conditions. Angle-resolved XPS further suggests that iridium at the surface is more reduced, while iridium in the bulk is more oxidized (Figure S10). Because TiO_2 stabilizes a higher iridium to oxygen ratio, it is reasonable that surface iridium, with fewer titanium neighbors, would be more reduced.

Phase separation in TiO_2−IrO_x alloys after annealing was investigated by grazing incidence X-ray diffraction (GIXRD). While nonalloyed ALD IrO_x showed peaks corresponding to metallic iridium after annealing (Figure S11), only a low intensity peak corresponding to anatase TiO_2 was occasionally observed for annealed TiO_2−IrO_x alloys (Figure S12). This is consistent with the beginnings of TiO_2 crystallization at 450 °C observed previously.[36] Analysis using a higher intensity X-ray source would improve the yield and resolution of diffraction peaks from such thin alloy films.

Alloys were also characterized by ultraviolet visible (UV−vis) spectroscopy to measure their absorption as a function of composition. The films became significantly more absorbing in the visible range of wavelengths as the % iridium increased to 43%.[37] Therefore, we focused further experimentation on lower (<43%) iridium content alloys.

2.2. Conductivity of TiO_2−IrO_x Alloys. In order to generate large photovoltages from *n*-Si, TiO_2−IrO_x alloys must be sufficiently conductive to induce a strong built-in field at the Si/SiO_2 interface. The conductivity of TiO_2−IrO_x alloy/SiO_2/p^+Si anodes was assessed by cyclic voltammetry, in which the peak-to-peak (P2P) splitting of the ferri/ferrocyanide (FFC) redox couple was measured as a function of alloy composition. The P2P splitting is simply the difference between the anodic and cathodic peak potentials ($E_{pa} - E_{pc}$). For a one-electron redox process, like the oxidation of Fe^{2+} to Fe^{3+}, the peak-to-peak splitting has a theoretical minimum of 57 mV.[38] Any increase in this value stems from uncompensated series resistance (in the solution or the anode) or slow electron transfer rates.

Figure 4A shows cyclic voltammograms in FFC for a series of 7 nm TiO_2−IrO_x alloy/SiO_2/p^+Si anodes compared to a 4 nm ALD IrO_x/SiO_2/p^+Si control. The P2P splitting of the ALD IrO_x/SiO_2/p^+Si anode was 169 mV. Electrochemical impedance measurements on both an ALD IrO_x/SiO_2/p^+Si anode and on a metallic gold electrode indicated that the uncompensated series resistance in 1 M KCl for our cell was 11−15 Ω cm^2 (Figure S13 and Table S5). As shown in Figure S14, a simulated cyclic voltammogram with an uncompensated series resistance of 14.9 Ω cm^2 replicated the experimental data quite well. Therefore, the peak-to-peak splitting exhibited by the ALD IrO_x control was roughly the minimum we could expect for this measurement.

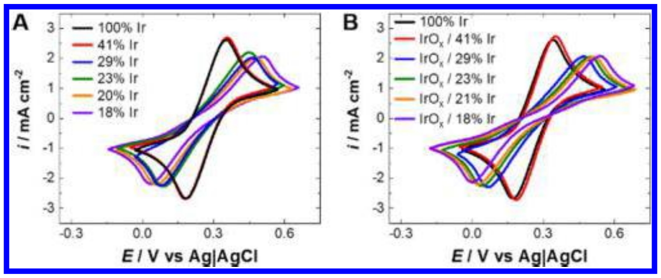

Figure 4. Cyclic voltammetry in 10 mM ferri/ferrocyanide, 1 M KCl in water of (A) 7 nm TiO_2−IrO_x alloy/SiO_2/p^+Si anodes and (B) ALD IrO_x-coated 7 nm TiO_2−IrO_x alloy/SiO_2/p^+Si anodes. A 4 nm ALD IrO_x/SiO_2/p^+Si anode (100% Ir) is also shown for comparison. All samples were annealed in forming gas (5% H_2/95% N_2) for 30 min at 450 °C. Cyclic voltammograms were measured in the dark at a scan rate of 100 mV/s.

The P2P splitting of the 41% alloy was equivalent to that of the ALD IrO_x control, but it increased significantly as the % Ir decreased. The increased P2P splitting could not be explained by increased charge transfer resistance, as TiO_2−IrO_x alloys coated with an additional layer of ALD IrO_x showed the same trend (Figure 4B). Instead, these data suggest the alloys themselves may contribute to the series resistance of the anode, with lower iridium content alloys displaying higher bulk resistance. This contrasts strongly with the behavior of TiO_2−RuO_2 alloys, which were highly conductive independent of ruthenium content down to 20% Ru.[7]

To understand the source of resistance in TiO_2−IrO_x/SiO_2/p^+Si anodes, we turned to electrochemical impedance spectroscopy (EIS). In this technique, an AC voltage is applied to the sample at open circuit, and the real and imaginary components of the impedance are measured over a range of AC frequencies. The AC response can be modeled by an equivalent circuit to understand the sources of resistance and capacitance. Data are visualized in a Nyquist plot, which shows the imaginary impedance as a function of the real impedance. Each point represents a different frequency.

Nyquist plots for a series of ALD IrO_x-coated alloys of composition 18−29% Ir are shown in Figure 5. Because the data were collected in 1 M H_2SO_4 at E_{OC}, no charge transfer is occurring. Under these conditions, the Nyquist plot for a purely metallic electrode should be a vertical line corresponding to the uncompensated series resistance (R_s) and double layer capacitance (C_{DL}) in series, yet this is not what we observed for TiO_2−IrO_x alloy electrodes. A vertical line appeared at low frequency, but the semicircle at higher

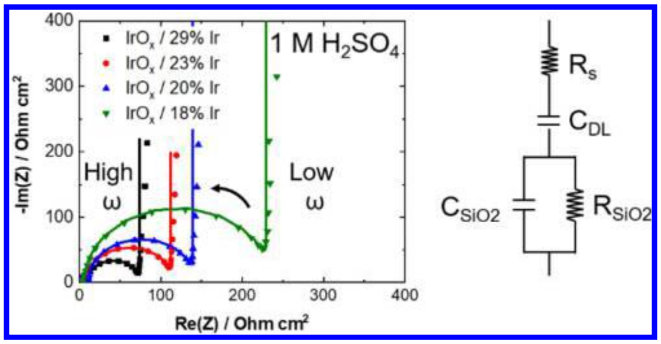

Figure 5. Nyquist plot for ALD IrO$_x$-coated 7 nm alloys ranging from 18 to 29% Ir collected at E_{OC} in 1 M H_2SO_4. All samples were annealed in forming gas (5% H_2/95% N_2) for 30 min at 450 °C. The frequency range was 200 mHz to 1 MHz. Symbols represent experimental data, and lines represent fitted data according to the equivalent circuit shown. In the model, R_{SiO2} is the tunnel resistance across the SiO_2, C_{SiO2} is the SiO_2 capacitance, C_{DL} is the double layer capacitance, and R_s is the uncompensated series resistance. Note that R_s is the sum of the uncompensated solution resistance and any bulk series resistance associated with charge transport through the alloy film.

frequencies indicated a parallel RC component. The parallel resistance (the width of the semicircle) depended strongly on the % Ir, but the parallel capacitance did not. Fitting this parallel RC component consistently yielded a capacitance of 1.3−1.4 μF cm^{-2}. This is the expected capacitance for a 2.5−2.6 nm SiO_2 film. To confirm that the high frequency capacitance was from the SiO_2, a 60% TiO_2−IrO_x alloy was deposited on p^+Si with a 5 nm SiO_2 layer. In this case, the high frequency capacitance was 0.64 μF cm^{-2},which translates to 5.4 nm SiO_2 (Table S6).

Thus, we propose the equivalent circuit model shown in Figure 5. The values of the fitted parameters are summarized in Table 2. At high frequency, we measure the tunnel resistance across the SiO_2 (R_{SiO2}) and the SiO_2 capacitance (C_{SiO2}) in parallel, connected in series with the uncompensated series resistance (R_s). As the iridium content in the alloy decreases, the density of states at the alloy/SiO_2 interface decreases, causing the tunnel resistance to increase. At low frequency, we probe the traditional double layer capacitance (C_{DL}) in series with the sum of R_{SiO2} and the uncompensated series resistance (R_s). It is important to note that R_S includes both the solution resistance and any bulk resistance of the alloy. For a 1 M H_2SO_4 solution in our cell, we expect a solution resistance of 3.5−4 Ω cm.[2] The values for R_s are 2−6 Ω cm^2 higher, indicating that the alloy might possess some bulk resistivity. The dominant barrier to charge transport through the MIS junction, however, is the SiO_2 tunnel resistance (R_{SiO2}).

Table 2. Summary of Fitted Parameters Corresponding to the Equivalent Circuit Model Shown in Figure 5[a]

% Ir	R_S (Ω cm^2)	C_{DL} (μF cm^{-2})	R_{SiO2} (Ω cm^2)	C_{SiO2} (μF cm^{-2})
18	5.9	116.8	223.6	1.3
20	10.2	117.4	128.9	1.4
23	8.1	124.9	104.5	1.4
29	8.6	112.9	65.0	1.3

[a] R_s is the uncompensated series resistance (solution resistance + bulk alloy resistance), C_{DL} is the double layer capacitance, R_{SiO2} is the tunnel resistance across the SiO_2, and C_{SiO2} is the capacitance across the SiO_2.

2.3. Photovoltage Generated by TiO_2−IrO_x Alloys.

Despite increased tunnelling resistance across the SiO_2, TiO_2−IrO_x alloys were still capable of generating large photovoltages from n-Si. The photovoltage was measured by cyclic voltammetry in 10 mM FFC, 1 M NaOH, pH 7 phosphate buffer, and 1 M H_2SO_4. In FFC, the photovoltage is taken to be the difference in potential between $E_{1/2}$ of p^+Si samples measured in the dark and $E_{1/2}$ of n-Si samples measured under 1 sun AM1.5 illumination, where $E_{1/2}$ is the average of the cathodic and anodic peak potentials ($[E_{pc}+ E_{pa}]/2$). In 1 M NaOH, pH 7 phosphate buffer, and 1 M H_2SO_4, the photovoltage is taken to be the difference in potential required to reach 1 mA cm^{-2} between p^+Si and n-Si samples.

Figure 6A shows the photovoltage of 7 nm 29% TiO_2−IrO_x alloy deposited on n-Si relative to a 4 nm ALD IrO_x control on p^+Si measured in FFC. The maximum photovoltage recorded was 638 mV for a 35% TiO_2−IrO_x alloy in FFC (Figure S15). The average photovoltage was 551 mV ± 60 mV, independent of iridium content across 11 alloy samples containing 18−35% iridium relative to titanium. The distribution of photovoltages is most likely because of uncontrolled variation in interface properties that could be avoided under more optimized alloy deposition conditions. Figure 6B−D shows representative water oxidation curves for the same alloy in 1 M NaOH, pH 7 phosphate buffer, and 1 M H_2SO_4. Photovoltages >500 mV were maintained in all three electrolytes. Figure 6E shows the saturated photocurrent density in 1 M H_2SO_4, which reached a value of 26 mA cm^{-2}. Although we do not know the exact optical constants of TiO_2−IrO_x alloys, we predict a saturated photocurrent density of 27 mA cm^{-2}[39] using reported optical constants for 5 nm TiO_2,[40] 2 nm Ir,[41] and 3 cm H_2O[42] (see Supporting Information).

TiO_2−IrO_x alloys possessed higher average photovoltages than the previously reported TiO_2−RuO_2 alloys.[7] The maximum 638 mV photovoltage recorded for TiO_2−IrO_x alloys is, to our knowledge, the highest reported photovoltage for a silicon MIS photoanode. Previous leading photovoltages include 570 mV achieved using ALD CoO_x on n-type silicon[13] 550 mV using PVD iridium on ultrathin ALD TiO_2 on n-type silicon after a forming gas anneal.[2] More recently, photovoltages up to 616 mV at 1 mA cm^{-1} were reported for TiO_2-protected n-Si photoanodes after annealing in forming gas to crystallize the TiO_2 into a higher-κ phase (rutile).[36] The 638 mV photovoltage obtained in this work is competitive with photovoltages obtained using buried p^+n homojunctions.[3]

Figure 6B−D also demonstrates the high overpotentials required for water oxidation on p^+Si samples. The thermodynamic potential for water oxidation in each electrolyte is indicated by the dashed line. Overpotentials of at least 400 mV were required to reach 1 mA cm^{-2}, and as shown in Figure 7A, the overpotential increased as the % iridium in the alloy decreased. A low density of iridium sites at the alloy/electrolyte interface was not responsible for these high overpotentials, as alloys coated with nominally 1 nm ALD IrO_x showed the same behavior (Figure 7B). Instead, the SiO_2 tunnel resistance limited the current density and contributed to higher overpotentials than would be expected for iridium at 1 mA cm^{-2}.

2.4. Corrosion Resistance of TiO_2−IrO_x Alloys.

Unlike TiO_2−RuO_2 alloys, we found that TiO_2−IrO_x alloys successfully prevented oxidation of the underlying silicon

DOI: 10.1021/acs.chemmater.8b03092
Chem. Mater. 2019, 31, 90−100

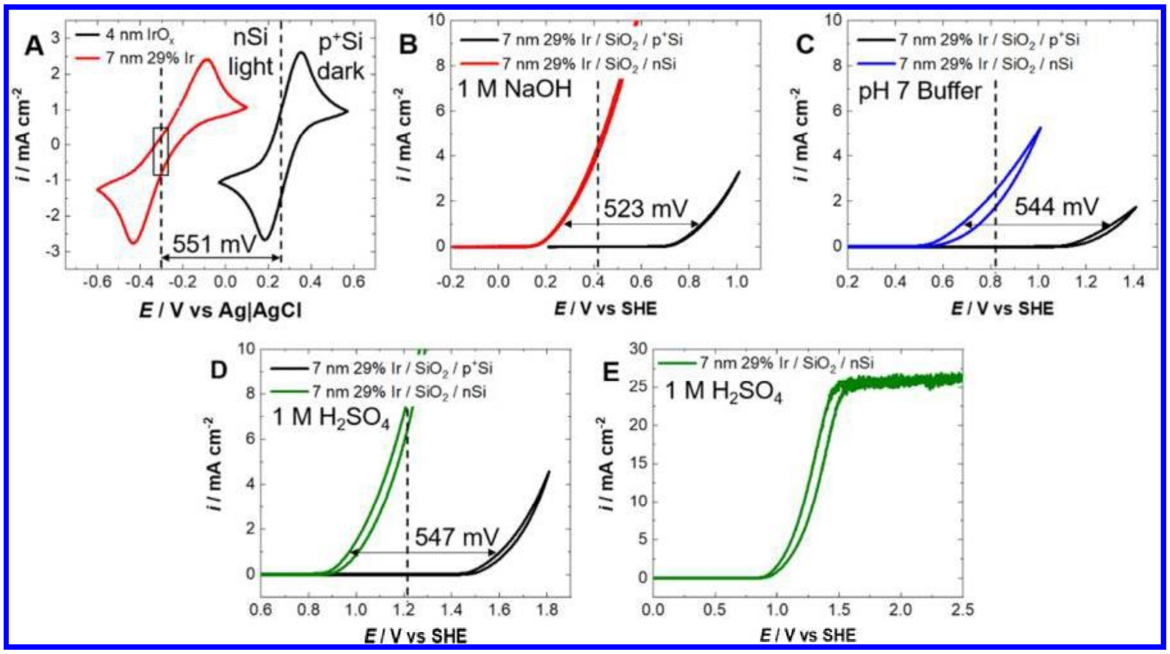

Figure 6. (A) Representative photovoltage of a 7 nm 29% TiO_2−IrO_x alloy on *n*-Si compared to a 4 nm ALD IrO_x film on p^+Si measured in 10 mM ferri/ferrocyanide, 1 M KCl. The average photovoltage for 11 samples ranging from 18 to 35% iridium was 551 mV, represented by the difference in potential between the two dashed lines. The box width represents the standard deviation of 60 mV. (B−D) Representative water oxidation data for the same 7 nm 29% TiO_2−IrO_x alloy on *n*-Si and p^+Si in 1 M NaOH, pH 7 phosphate buffer, and 1 M H_2SO_4. The dashed lines indicate the thermodynamic potential for oxygen evolution at each pH. (E) Saturated photocurrent density for the 7 nm 29% TiO_2−IrO_x alloy in 1 M H_2SO_4. All samples were annealed in forming gas (5% H_2/95% N_2) for 30 min at 450 °C. All *n*-Si samples were measured under AM1.5 simulated solar radiation. The scan rate for all measurements was 100 mV/s.

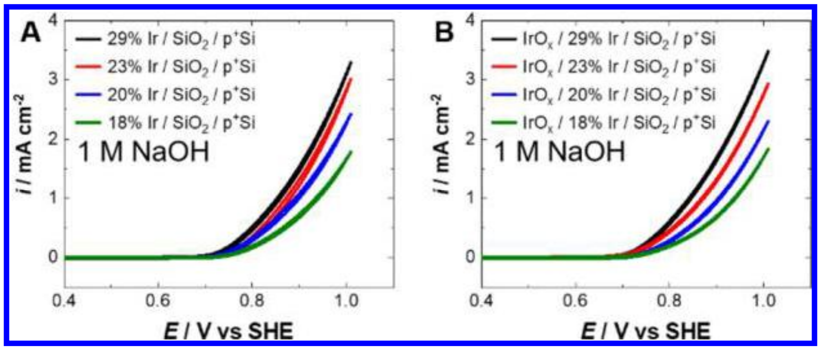

Figure 7. Water oxidation in 1 M NaOH for (A) 7 nm TiO_2−IrO_x alloys ranging from 18% to 29% Ir and (B) IrO_x-coated 7 nm TiO_2−IrO_x alloys ranging from 18% to 29% Ir. All samples were deposited on p^+Si and annealed in forming gas (5% H_2/95% N_2) for 30 min at 450 °C. Cyclic voltammograms were measured in the dark at a scan rate of 100 mV/s.

substrate. Corrosion resistance of TiO_2−IrO_x alloys was assessed by measuring the SiO_2 thickness before and after long-term water oxidation. Because EIS probes the SiO_2 capacitance and tunnel resistance at high frequency, any changes in the SiO_2 thickness will manifest as changes in C_{SiO2} and R_{SiO2}. Because of the complexity of EIS on *n*-Si samples with potential-dependent depletion layers or possible inversion layers, long-term stability tests were primarily conducted on p^+Si, for which the capacitance assigned to the SiO_2 layer (and therefore its thickness) can be readily determined by EIS. However, long-term stability tests under AM1.5 simulated solar radiation behaved similarly. An example is shown in Figure S16.

As shown in Figure 8A, TiO_2−IrO_x alloys on p^+Si were held at 1.8 V vs SHE for 12 h of continuous water oxidation in 1 M H_2SO_4. Water oxidation current decayed significantly over the first several hours of testing. Some of this decay may be related to iridium loss at the alloy/electrolyte interface. XPS analysis of a 7 nm TiO_2−IrO_x alloy after 12 h of continuous water oxidation showed a decrease in the iridium content from 32% to 24% iridium (Figure S18A). Losing 33% of the iridium content at the electrode surface, however, is unlikely to be responsible for the total current loss, which can approach 86% over the course of 12 h.

Instead, the long-term decrease in current density may also be related to the catalytic activity of iridium, which is known to depend strongly on its oxidation state and chemical environment.[27,43−46] Hydrated forms of IrO_x are generally more active than IrO_2,[27,43−46] and prolonged exposure to positive potentials can reduce the catalytic activity of hydrated IrO_x by converting it to a less active, dry IrO_2. Rutile IrO_2 generally shows the lowest catalytic activity,[43,45,46] but catalytic activity is strongly related to the degree of hydration regardless of crystallinity.[43,45] Our results show a similar trend: as the

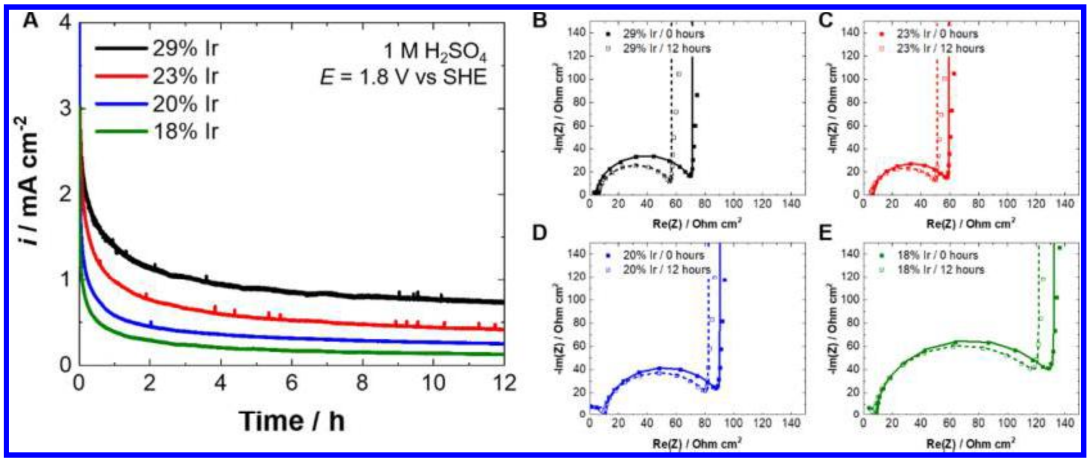

Figure 8. (A) Water oxidation current as a function of time for TiO_2−IrO_x alloys/SiO_2/p^+Si measured in the dark. All samples were annealed in forming gas (5% H_2/95% N_2) for 30 min at 450 °C prior to testing. Samples were held at a potential of 1.8 V vs SHE in 1 M H_2SO_4 for 12 h. (B−E) Nyquist plots for each alloy before and after 12 h of continuous water oxidation in 1 M H_2SO_4. Symbols represent experimental data and lines represent fits according to the equivalent circuit model proposed in Figure 5. The dashed lines represent fits to the data after 12 h of testing.

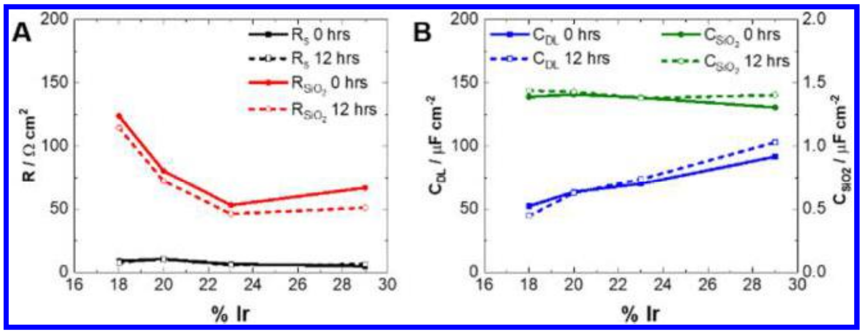

Figure 9. (A) Series resistance (R_S) and SiO_2 tunnel resistance (R_{SiO2}) before and after 12 h of testing in 1 M H_2SO_4 at E = 1.8 V vs SHE. (B) Double layer capacitance (C_{DL}) and SiO_2 capacitance (C_{SiO2}) before and after 12 h of testing. Impedance data was collected at E_{OC} over a frequency range of 200 mHz−1 MHz and values were extracted according to the equivalent circuit model shown in Figure 5. Solid lines were collected before testing, dashed lines were collected after continuous water oxidation in 1 M H_2SO_4 for 12 h. All samples were annealed in forming gas (5% H_2/95% N_2) for 30 min at 450 °C prior to testing.

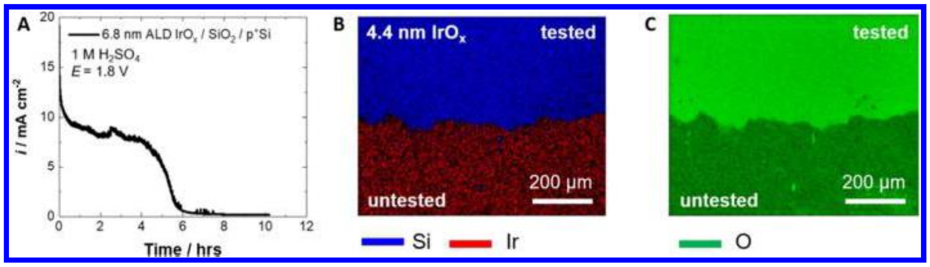

Figure 10. (A) Chronoamperometry measurement for a 6.8 nm ALD IrO_x film in 1 M H_2SO_4 with an applied potential of 1.8 V vs SHE. (B) Auger electron spectroscopy map for silicon and iridium on the tested and untested regions of the sample in panel A. (C) Auger electron spectroscopy map for oxygen on the same tested and untested regions. All samples were annealed in forming gas (5% H_2/95% N_2) for 30 min at 450 °C.

potential is held at highly positive potentials, the current decreases as more and more IrO_x is converted to inactive IrO_2.

The current density also increased as the % Ir in the alloy increased. This effect was true even for alloys coated with an additional layer of ALD IrO_x (Figure S17), which suggests that the density of Ir ions at the alloy/electrolyte interface is not limiting the current density. Based on the previously described equivalent circuit model, it is more likely that the SiO_2 tunnel resistance limits the final current density. Higher % Ir alloys sustained higher current densities because the higher effective density of states at the alloy/SiO_2 interface reduced the tunnelling resistance. In other words, although the applied potential was the same, the effective potential across the alloy/electrolyte interface was lower for low % Ir alloys.

Figure 8B−E shows the impedance spectra collected before and after testing, and Figure 9 summarizes the fitted R_S, R_{SiO2}, C_{DL}, and C_{SiO2}. R_s and C_{DL} remained constant before and after testing, which suggests no major changes to the alloy/electrolyte interface or to the bulk conductivity of the alloy. C_{SiO2} remained constant as well, which indicates no SiO_2 growth. R_{SiO2} decreased slightly after the stability test, possibly because the iridium oxidation state increased after testing. E_{OC} increased from 0.7 V vs SHE to nearly 0.9 V vs SHE, and XPS indicated Ir oxidation, as well (Figure S18A).

The tunnelling resistance likely depends not only on the iridium concentration but also on the chemical nature of the iridium atoms near the SiO_2 layer. While the iridium oxidation state might change, there is no evidence of iridium loss from the SiO_2/alloy interface.

To understand the role that TiO_2 plays in stabilizing TiO_2-IrO_x alloys during water oxidation, nonalloyed ALD IrO_x was subjected to the same 12 h of testing at 1.8 V vs SHE in 1 M H_2SO_4. As shown in Figure 10A, the water oxidation current was much higher for nonalloyed ALD IrO_x deposited directly on SiO_2/silicon, even though the applied potential and electrolyte concentration were the same. This is because the SiO_2 tunnelling resistance is small when ALD IrO_x is used as the Schottky contact compared to TiO_2-IrO_x alloys. Despite higher initial current densities, nonalloyed IrO_x failed after just 4−6 h of testing. Analysis by Auger electron spectroscopy indicated that no iridium was present on the anode surface after the stability test (Figure 10B). Oxygen enrichment in the tested region (Figure 10C) further suggests growth of a thick SiO_2, in accordance with previous observations.[2] XPS analysis of the tested region of a 7 nm 32% TiO_2-IrO_x alloy coated anode showed that iridium was still present, as shown in Figure S19A. No Si 2p substrate peaks were observed (Figure S18B), indicating that the film thickness did not decrease below the inelastic mean free path for Si 2p electrons (~1.7 nm in pure Ir). The Ir 4f peak of the tested region showed a distinct component at higher binding energy, indicative of Ir oxidation. The intensity of the Ir 4f peak was lower, however, and the Ir content dropped from 32% to 24% Ir relative to Ti. Iridium loss likely occurred at the alloy surface because EIS suggests little change at the SiO_2/alloy interface after the chronoamperometry stability test.

TiO_2 alloying clearly improved the stability of iridium during water oxidation. Thermodynamically, IrO_2 should be stable up to 1.6 V vs SHE.[47] Iridium dissolution above 1.6 V vs SHE has been extensively studied,[48−50] and more recently, iridium dissolution has been observed at potentials as low as 1.0−1.2 V vs SHE.[51,52] Iridium loss from the surface of TiO_2-IrO_x alloys could be related to the ALD alloying sequence. The last cycle in any ALD supercycle is an IrO_x cycle. We suspect this final layer of iridium is more susceptible to corrosion than iridium in the bulk, which is surrounded by stabilizing titanium atoms. Regardless, alloying iridium with TiO_2 is a promising approach for improving the stability of IrO_x during water oxidation, even at potentials up to 1.8 V vs SHE. A similar effect was observed for the analogous TiO_2/IrO_2 dimensionally stable anode used for oxygen evolution.[53]

The improved stability of TiO_2-IrO_x alloys compared to TiO_2-RuO_2 alloys is most likely related to the improved thermodynamic stability of IrO_2 under water oxidation conditions. While IrO_2 is stable up to 1.6 V vs SHE,[47] RuO_2 oxidizes to volatile RuO_4 at 1.4 V vs SHE.[54] Alloying with TiO_2 cannot overcome the strong driving force for RuO_2 oxidation, but IrO_2 is more easily stabilized.

3. CONCLUSIONS

Alloying TiO_2 with a high work function metal oxide is a promising strategy for maximizing the voltage generated by photoanode devices, particularly those based on semiconductors that cannot be doped to form buried p^+n homojunctions. TiO_2 imparts corrosion resistance, while the high work function metal oxide enables high photovoltage, high conductivity, and catalytic activity. By replacing the ruthenium in TiO_2-RuO_2 alloys with iridium, we significantly improved the stability of these Schottky contacts. TiO_2-IrO_x alloys as the metal layer in nSi/SiO_2 MIS Schottky junctions generated photovoltages greater than 600 mV, while simultaneously functioning as water oxidation catalysts and corrosion resistant coatings. EIS confirmed no change in the SiO_2 thickness after 12 h of continuous water oxidation in 1 M H_2SO_4. We also found that the density of states at the insulator/metal interface played a key role in charge transport through the junction. Thinning the insulator layer or increasing the metal content at the alloy/SiO_2 interface could minimize this resistance in the future. The ability to create graded structures by ALD presents a unique opportunity to control the composition as a function of depth, placing valuable metal atoms where they are needed most: at the electrode/electrolyte interface for catalysis and at the insulator/metal interface for efficient tunneling.

4. MATERIALS AND METHODS

4.1. Silicon Substrates. Heavily boron-doped (100) *p*-type silicon wafers (ρ = 0.001−0.002 Ω cm, thickness 505−545 μm) were used as conductive silicon substrates for electrochemical measurements in the dark. Moderately phosphorus-doped (100) *n*-type silicon wafers (ρ = 0.14−0.24 Ω cm, thickness 450 μm) were employed for electrochemical measurements in the light. The wafers were used as-received with a 2 nm vendor-supplied chemical oxide (SiO_2) layer, as measured by ellipsometry prior to deposition.

4.2. Atomic Layer Deposition (ALD). All ALD films were deposited in a custom-built ALD reactor, described previously.[7] Tetrakis(dimethylamido)titanium (TDMAT) was used as the titanium precursor and water as the coreactant.[19] The TDMAT bubbler was kept at 45 °C and the water bubbler was kept at room temperature. The substrate temperature was approximately 175 °C, within the ALD window for the TDMAT system.[19,55] The TDMAT pulse time was 3 s and the H_2O pulse time was 0.5 s. N_2 at 50 sccm was used as the purge gas for 30 s between each reactant pulse. The deposition pressure was 300 mTorr.

IrO_x films were grown using 1-ethylcyclopentadienyl-1,3-cyclohexadiene iridium(I) ((EtCp)Ir(CHD)) and ozone.[20] (EtCp)Ir(CHD) was purchased from Strem Chemical. This precursor was chosen because its low temperature ALD window overlaps with that of TDMAT. Ozone was generated using an Orec Laboratory Ozone Generator, Model #V10-O. The ozone output was measured to be 14.8 g m^{-3} using an in-line MINI-HICON benchtop ozone analyzer. The (EtCp)Ir(CHD) bubbler was kept at 45 °C. (EtCp)Ir(CHD) is a liquid with a low vapor pressure, so N_2 at 50 sccm was used as a carrier gas. As with the TiO_2 process, N_2 at 50 sccm was used as the purge gas for 30 s between each reactant pulse. The deposition pressure was approximately 300 mTorr. The (EtCp)Ir(CHD) pulse time was 3 s and the O_3 pulse time was 3 s.

To grow TiO_2-IrO_x alloys, alternating cycles of TiO_2 and IrO_x were repeated for a specified number of supercycles. The ratio of TiO_2 cycles to IrO_x cycles controlled the Ir content in the film. The number of supercycles controlled the overall film thickness. All deposition conditions for the alloys were the same as those used in ALD of films of the individual metal oxide components IrO_x and TiO_2. The specific pulse sequence can be found in Table S1 of the Supporting Information.

4.3. Determination of ALD IrO_x and Alloy Film Thickness by X-ray Reflectivity (XRR). IrO_x and alloy film thicknesses were measured by XRR using a PANalytical X'Pert diffractometer. The incident beam optics included a graded multilayer parabolic X-ray mirror, a 1/32° divergence slit, a 10 mm mask for smaller samples, and a Ni 0.15 mm automatic beam attenuator. The scattered beam optics included a parallel plate collimator with a 0.27° receiving slit. PANalytical's X'Pert reflectivity software was used to calculate film thickness from a 2Theta-Omega scan using the Fourier transform method. Scans were collected over the range of scattering angles $2\theta = 0-8°$. The step size was 0.02° and the time per step was 3.0 s.

4.4. Determination of Crystal Structure by Grazing Incidence X-ray Diffraction (GIXRD). GIXRD spectra were collected on a PANalytical X'Pert diffractometer. The X-ray source was monochromatic Cu $K\alpha_1$ with a wavelength of 1.540 56 Å. The incident beam optics included a graded multilayer parabolic X-ray mirror (the monochromator), a 1/2° divergence slit, a 15 mm mask for smaller samples, and a Ni 0.15 mm automatic beam attenuator. The diffracted beam optics included a parallel plate collimator. No receiving slit was used in order to maximize the signal intensity. Scans were collected over the range $2\theta = 20-80°$ with $\omega = 2.5$.° The step size was 0.05° with a time per step of 1 s.

4.5. Deposition of Black Contact. 100 nm Al was used as the back contact for *n*-Si wafers, and 20 nm Pt was used as the back contact for p^+Si wafers. Both were deposited by electron beam evaporation.

4.6. X-ray Photoelectron Spectroscopy (XPS). Elemental characterization of ALD films was performed using a PHI 5000 VersaProbe X-ray photoelectron spectrometer. The chamber base pressure was typically on the order of 10^{-7} Torr. The X-ray source was monochromatic Al $K\alpha$ (1486.6 eV). The power to the X-ray source was 50 W, and the beam diameter was focused to 200 μm. The photoelectron takeoff angle 45°. For survey scans, the pass energy was 117.4 eV with an energy step of 1.0 eV. For high resolution scans, the pass energy was 23.5 eV with an energy step of 0.10 eV. Pass energies were chosen based on the manufacturer recommendation to maximize either electron yield or energy resolution. The time/step was 20 ms in all cases.

CasaXPS software was used for elemental analyses and peak fitting. All peak positions were referenced to the C 1s peak at 284.5 eV. Relative sensitivity factors for each element were taken from the PHI Multipak Manual.

4.7. Electrochemical Measurements. Aqueous ferri/ferrocyanide solution (10 mM FFC) was made with 10 mM $K_3Fe(CN)_6$, 10 mM K4Fe$(CN)_6$, and 1 M KCl in deionized water. ACS Certified sodium hydroxide pellets, potassium chloride, and concentrated sulfuric acid were purchased from Fisher Chemical. The pH 7 phosphate buffer solution was made with 0.42 M anhydrous Na_2HPO_4 and 0.58 M monohydrate $NaH_2PO_4\cdot H_2O$, both purchased from RICCA Chemical Company. All electrochemical measurements were performed using a bored (5 mm diameter, 0.196 cm^2 area) Teflon cone pressed against the sample to define the electrode area and contain the electrolyte solution. A Pt wire was used as a counter electrode. A Ag(s)lAgCl(s) sat. KCl (aq) electrode purchased from Bioanalytical Systems was the reference electrode. Potentials measured versus AglAgCl were converted to SHE. All measurements were conducted using a Biologic SP-200 potentiostat in air at room temperature. Cyclic voltammograms were recorded at a scan rate of 100 mV s^{-1}. Chronoamperometry measurements were performed using a peristaltic pump to circulate the solution within the bore at 1 mL s^{-1}. Unless otherwise stated, impedance measurements were recorded from 200 mHz to 1 MHz at 6 points per decade with an AC amplitude of 10 mV. Two measurements were taken per frequency.

4.8. Auger Electron Spectroscopy (AES) Mapping. AES maps were collected using a PHI 700 Auger electron spectrometer. The beam energy was 10.0 kV with 8.5 nA current. A 2-point acquisition method was used with a resolution of 128 pixels.

ASSOCIATED CONTENT

Ⓢ Supporting Information

The Supporting Information is available free of charge on the ACS Publications website at DOI: 10.1021/acs.chemmater.8b03092.

Detailed methods and analysis for XPS, XRR, GIXRD, and electrochemical impedance spectroscopy; detailed description of ALD pulse sequences involved in TiO_2-IrO_x alloy deposition; discussion of the effect of forming gas annealing on stability (PDF)

AUTHOR INFORMATION

Corresponding Authors

*C. E. D. Chidsey. Email: chidsey@stanford.edu.
*P. C. McIntyre. Email: pcm1@stanford.edu.

ORCID

Robert Tang-Kong: 0000-0003-4583-460X
Christopher E. D. Chidsey: 0000-0001-8217-0393

Author Contributions

O.H. prepared all samples and performed all experiments for this study. O.H., C.E.D.C., and P.C.M. designed the experiments. At the time of this publication, modification of the catalytic properties of IrO_2 by small thickness ALD-TiO_2 layers has recently been reported.[56]

Funding

NSF RENEW program, award no. CBET-1336844 NSF EMERALD program; award no: CBET-1805084 NSF ECCS-1542152.

Notes

The authors declare no competing financial interest.

ACKNOWLEDGMENTS

Part of this work was performed at the Stanford Nano Shared Facilities (SNSF), supported by the National Science Foundation under award ECCS-1542152. We thank T. Carver for metal e-beam evaporations. O.H. thanks C. Hitzman for his guidance with XPS and AES. We also acknowledge A. Vailionis for his help with XRR and GIXRD measurements. This work was partially supported by the NSF RENEW program, award no. CBET-1336844 and the NSF EMERALD program, award no. CBET 1805084. O.H. graciously acknowledges support from the Fannie and John Hertz Foundation.

REFERENCES

(1) Godfrey, R. B.; Green, M. A. 655 MV Open-Circuit Voltage, 17.6% Efficient Silicon MIS Solar Cells. *Appl. Phys. Lett.* **1979**, *34* (11), 790−793.

(2) Chen, Y. W.; Prange, J. D.; Dühnen, S.; Park, Y.; Gunji, M.; Chidsey, C. E. D.; McIntyre, P. C. Atomic Layer-Deposited Tunnel Oxide Stabilizes Silicon Photoanodes for Water Oxidation. *Nat. Mater.* **2011**, *10* (7), 539−544.

(3) Scheuermann, A. G.; Lawrence, J. P.; Kemp, K. W.; Ito, T.; Walsh, A.; Chidsey, C. E. D.; Hurley, P. K.; McIntyre, P. C. Design Principles for Maximizing Photovoltage in Metal-Oxide-Protected Water-Splitting Photoanodes. *Nat. Mater.* **2016**, *15*, 99−105.

(4) Singh, R.; Green, M. A.; Rajkanan, K. Review of Conductor-Insulator-Semiconductor (CIS) Solar Cells. *Sol. Cells* **1981**, *3*, 95−148.

(5) Green, M. A. Limits on the Open-Circuit Voltage and Efficiency of Silicon Solar Cells Imposed by Intrinsic Auger Processes. *IEEE Trans. Electron Devices* **1984**, *31* (5), 671−678.

(6) Green, M. A.; Blakers, A. W. Advantages of Metal-Insulator-Semiconductor Structure for Silicon Solar Cells. *Sol. Cells* **1983**, *8*, 3−16.

(7) Hendricks, O. L.; Scheuermann, A. G.; Schmidt, M.; Hurley, P. K.; McIntyre, P. C.; Chidsey, C. E. D. Isolating the Photovoltaic Junction : Atomic Layer Deposited TiO2 − RuO2 Alloy Schottky Contacts for Silicon Photoanodes. *ACS Appl. Mater. Interfaces* **2016**, *8*, 23763−23773.

(8) Digdaya, I. A.; Trześniewski, B. J.; Adhyaksa, G. W. P.; Garnett, E. C.; Smith, W. A. General Considerations for Improving

Photovoltage in Metal-Insulator-Semicondutor Photoanodes. *J. Phys. Chem. C* **2018**, *122*, 5462−5471.

(9) Green, M. A.; Godfrey, R. B. MIS Solar Cell — General Theory and New Experimental Results for Silicon. *Appl. Phys. Lett.* **1976**, *29*, 610−612.

(10) Green, M. A.; King, F. D.; Shewchun, J. Minority Carrier MIS Tunnel Diodes and Their Application to Electron- and Photo-Voltaic Energy Conversion-I Theory. *Solid-State Electron.* **1974**, *17*, 551−561.

(11) Godfrey, R. B.; Green, M. A. High-Efficiency Silicon MinMIS Solar Cells—Design and Experimental Results. *IEEE Trans. Electron Devices* **1980**, *27* (4), 737−745.

(12) Card, H. C.; Yang, E. S. MIS-Schottky Theory under Conditions of Optical Carrier Generation in Solar Cells. *Appl. Phys. Lett.* **1976**, *29*, 51−53.

(13) Zhou, X.; Liu, R.; Sun, K.; Papadantonakis, K. M.; Brunschwig, B. S.; Lewis, N. 570 MV Photovoltage, Stabilized n-Si/CoOx Heterojunction Photoanodes Fabricated Using Atomic Layer Deposition. *Energy Environ. Sci.* **2016**, *9*, 892−897.

(14) Zhou, X.; Liu, R.; Sun, K.; Friedrich, D.; McDowell, M. T.; Yang, F.; Omelchenko, S. T.; Saadi, F. H.; Nielander, A. C.; Yalamanchili, S.; et al. Interface Engineering of the Photoelectrochemical Performance of Ni-Oxide-Coated n-Si Photoanodes by Atomic-Layer Deposition of Ultrathin Films of Cobalt Oxide. *Energy Environ. Sci.* **2015**, *8*, 2644−2649.

(15) Kenney, M. J.; Gong, M.; Li, Y.; Wu, J. Z.; Feng, J.; Lanza, M.; Dai, H. High-Performance Silicon Photoanodes Passivated with Ultrathin Nickel Films for Water Oxidation. *Science (Washington, DC, U. S.)* **2013**, *342*, 836−840.

(16) Scheuermann, A. G.; McIntyre, P. C. Atomic Layer Deposited Corrosion Protection: A Path to Stable and Efficient Photoelectrochemical Cells. *J. Phys. Chem. Lett.* **2016**, *7* (14), 2867−2878.

(17) Hu, S.; Shaner, M. R.; Beardslee, J. A.; Lichterman, M.; Brunschwig, B. S.; Lewis, N. S. Amorphous TiO2 Coatings Stabilize Si, GaAs, and GaP Photoanodes for Efficient Water Oxidation. *Science (Washington, DC, U. S.)* **2014**, *344*, 1005−1009.

(18) McDowell, M. T.; Lichterman, M. F.; Carim, A. I.; Liu, R.; Hu, S.; Brunschwig, B. S.; Lewis, N. S. The Influence of Structure and Processing on the Behavior of TiO_2 Protective Layers for Stabilization of n-Si/TiO_2 /Ni Photoanodes for Water Oxidation. *ACS Appl. Mater. Interfaces* **2015**, *7* (28), 15189−15199.

(19) Scheuermann, A. G.; Lawrence, J. P.; Gunji, M.; Chidsey, C. E. D.; McIntyre, P. C. ALD-TiO2 Preparation and Characterization for Metal-Insulator-Silicon Photoelectrochemical Applications. *ECS Trans.* **2013**, *58* (10), 75−86.

(20) Hämäläinen, J.; Hatanpää, T.; Puukilainen, E.; Sajavaara, T.; Ritala, M.; Leskelä, M. Iridium Metal and Iridium Oxide Thin Films Grown by Atomic Layer Deposition at Low Temperatures. *J. Mater. Chem.* **2011**, *21*, 16488−16493.

(21) Hämäläinen, J.; Hatanpää, T.; Puukilainen, E.; Costelle, L.; Pilvi, T.; Ritala, M.; Leskelä, M. (MeCp)Ir(CHD) and Molecular Oxygen as Precursors in Atomic Layer Deposition of Iridium. *J. Mater. Chem.* **2010**, *20*, 7669−7675.

(22) Pfeifer, V.; Jones, T. E.; Velasco Velez, J. J.; Massue, C.; Arrigo, R.; Teschner, D.; Girgsdies, F.; Scherzer, M.; Greiner, M. T.; Allan, J.; et al. The Electronic Structure of Iridium and Its Oxides. *Surf. Interface Anal.* **2016**, *48* (5), 261−273.

(23) Bozack, M. J. Sputter-Induced Modifications of IrO2 During XPS Measurements. *Surf. Sci. Spectra* **1993**, *2*, 123−127.

(24) Gaarenstroom, S. W.; Winograd, N. Initial and Final State Effects in the ESCA Spectra of Cadmium and Silver Oxides Initial and Final State Effects in the ESCA Spectra of Cadmium and Silver Oxides. *J. Chem. Phys.* **1977**, *67* (8), 3500−3506.

(25) Abbott, D. F.; Lebedev, D.; Waltar, K.; Povia, M.; Nachtegaal, M.; Fabbri, E.; Coperet, C.; Schmidt, T. J. Iridium Oxide for the Oxygen Evolution Reaction: Correlation between Particle Size, Morphology, and the Surface Hydroxo Layer from Operando XAS. *Chem. Mater.* **2016**, *28*, 6591−6604.

(26) Smith, R. D. L.; Sporinova, B.; Fagan, R. D.; Trudel, S.; Berlinguette, C. P. Facile Photochemical Preparation of Amorphous Iridium Oxide Films for Water Oxidation Catalysis. *Chem. Mater.* **2014**, *26* (4), 1654−1659.

(27) Pfeifer, V.; Jones, T. E.; Velasco Velez, J. J.; Massué, C.; Greiner, M. T.; Arrigo, R.; Teschner, D.; Girgsdies, F.; Scherzer, M.; Allan, J.; et al. The Electronic Structure of Iridium Oxide Electrodes Active in Water Splitting. *Phys. Chem. Chem. Phys.* **2016**, *18*, 2292−2296.

(28) Ito, S.; Abe, Y.; Kawamura, M.; Kim, K. H. Electrochromic Properties of Iridium Oxide Thin Films Prepared by Reactive Sputtering in O2 or H2O Atmosphere. *J. Vac. Sci. Technol., B: Nanotechnol. Microelectron.: Mater., Process., Meas., Phenom.* **2015**, *33*, 41204.

(29) Cruz, A. M.; Abad, L.; Carretero, N. M.; Moral-Vico, J.; Fraxedas, J.; Lozano, P.; Subias, G.; Padial, V.; Carballo, M.; Collazos-Castro, J. E.; et al. Iridium Oxohydroxide, a Significant Member in the Family of Iridium Oxides. Stoichiometry, Characterization, and Implications in Bioelectrodes. *J. Phys. Chem. C* **2012**, *116* (8), 5155−5168.

(30) Atanasoska, L.; Gupta, P.; Deng, C.; Warner, R.; Larson, S.; Thompson, J. XPS, AES, and Electrochemical Study of Iridium Oxide Coating Materials for Cardiovascular Stent Application. *ECS Trans.* **2008**, *16* (38), 37−48.

(31) Diebold, U.; Madey, T. E. TiO2 by XPS. *Surf. Sci. Spectra* **1996**, *4* (3), 227−231.

(32) Abbott, D. F.; Lebedev, D.; Waltar, K.; Povia, M.; Nachtegaal, M.; Fabbri, E.; Copéret, C.; Schmidt, T. J. Iridium Oxide for the Oxygen Evolution Reaction: Correlation between Particle Size, Morphology and the Surface Hydroxo Layer from Operando XAS. *Chem. Mater.* **2016**, *28*, 6591−6604.

(33) Beamson, G.; Briggs, D. *High Resolution XPS of Organic Polymers, the Scienta ESCA300 Database*; Wiley: Chichester, 1993.

(34) McIntyre, N. S.; Chan, T. C. *Practical Surface Analysis*, Vol. *1*.; Briggs, D., Seah, M. P., Eds.; Wiley: New York, 1990.

(35) McCafferty, E.; Wightman, J. P. Determination of the Concentration of Surface Hydroxyl Groups on Metal Oxide Films by a Quantitative XPS Method. *Surf. Interface Anal.* **1998**, *26*, 549−564.

(36) Scheuermann, A. G.; Lawrence, J. P.; Meng, A. C.; Tang, K.; Hendricks, O. L.; Chidsey, C. E. D.; McIntyre, P. C. Titanium Oxide Crystallization and Interface Defect Passivation for High Performance Insulator-Protected Schottky Junction MIS Photoanodes. *ACS Appl. Mater. Interfaces* **2016**, *8* (23), 14596−14603.

(37) Tan, W.; Hendricks, O. L.; Meng, A. C.; Braun, M. R.; McGehee, M. D.; Chidsey, C. E. D.; McIntyre, P. C. Atomic Layer Deposited TiO2-IrOx Alloy as a Hole Transport Material for Perovskite Solar Cells. *Adv. Mater. Interfaces* **2018**, *5*, 1800191.

(38) Bard, A. J.; Faulkner, L. R. *Electrochemical Methods*, Second ed.; John Wiley & Sons: New York, 2001.

(39) McIntosh, K. R.; Baker-Finch, S. C. OPAL 2: Rapid Optical Simulation of Silicon Solar Cells. *Conf. Rec. IEEE Photovolt. Spec. Conf.* 2012, 265−271.

(40) Richards, B. Single-Material TiO2 Double-Layer Antireflection Coatings. *Sol. Energy Mater. Sol. Cells* **2003**, *79*, 369−390.

(41) Yan, L.; Woollam, J. A. Optical Constants and Roughness Study of Dc Magnetron Sputtered Iridium Films. *J. Appl. Phys.* **2002**, *92* (8), 4386−4392.

(42) Irvine, W. M.; Pollack, J. B. Infrared Optical Properties of Water and Ice Spheres. *Icarus* **1968**, *8*, 324−360.

(43) Jovanovic, P.; Hodnik, N.; Ruiz-zepeda, F.; Arcon, I.; Jozinovic, B.; Zorko, M.; Bele, M.; Sala, M.; Selih, V. S.; Hocevar, S.; et al. Electrochemical Dissolution of Iridium and Iridium Oxide Particles in Acidic Media: Transmission Electron Microscopy, Electrochemical Flow Cell Coupled to Inductively Coupled Plasma Mass Spectrometry, and X - Ray Absorption Spectroscopy Study. *J. Am. Chem. Soc.* **2017**, *139* (36), 12837−12846.

(44) Minguzzi, A.; Lugaresi, O.; Achilli, E.; Locatelli, C.; Vertova, A.; Ghigna, P.; Rondinini, S. Observing the Oxidation State Turnover in Heterogeneous Iridium-Based Water Oxidation Catalysts. *Chem. Sci.* **2014**, *5*, 3591−3597.

(45) Minguzzi, A.; Locatelli, C.; Lugaresi, O.; Achilli, E.; Cappelletti, G.; Scavini, M.; Coduri, M.; Masala, P.; Sacchi, B.; Vertova, A.; et al. Easy Accommodation of Different Oxidation States in Iridium Oxide Nanoparticles with Different Hydration Degree as Water Oxidation Electrocatalysts. *ACS Catal.* **2015**, *5*, 5104−5115.

(46) Pfeifer, V.; Jones, T. E.; Wrabetz, S.; Velasco Velaz, J. J.; Arrigo, R.; Scherzer, M.; Piccinin, S.; Massue, C.; Havecker, M.; Knop-Gericke, A. Reactive Oxygen Species in Iridium-Based OER Catalysts. *Chem. Sci.* **2016**, *7*, 6791−6795.

(47) Pourbaix, M. *Atlas of Electrochemical Equilibria in Aqueous Solutions*; Pergamon Press: Oxford, NY, 1966.

(48) Gottesfeld, S.; McIntyre, J. D. E.; Beni, G.; Shay, J. L.; Gottesfeld, S.; McIntyre, J. D. E. Electrochromism in Anodic Iridium Oxide Films Electrochromism in Anodic Iridium. *Oxide Films.* **2016**, *208* (1978), 2−5.

(49) Buckley, D. N.; Burke, L. D. The Oxygen Electrode Part 5. Enhancement of Charge Capacity of an Iridium Surface in the Anodic Region. *J. Chem. Soc., Faraday Trans. 1* **1975**, *71*, 1447−1459.

(50) Buckley, D. N.; Burke, L. D. The Oxygen Electrode Part 6. Oxygen Evolution and Corrosion at Iridium Anodes. *J. Chem. Soc., Faraday Trans. 1* **1976**, *72*, 2431−2440.

(51) Cherevko, S.; Geiger, S.; Kasian, O.; Mingers, A.; Mayrhofer, K. J. J. Oxygen Evolution Activity and Stability of Iridium in Acidic Media. Part 1. − Metallic Iridium. *JEAC* **2016**, *773*, 69−78.

(52) Cherevko, S.; Geiger, S.; Kasian, O.; Mingers, A.; Mayrhofer, K. J. J. Oxygen Evolution Activity and Stability of Iridium in Acidic Media. Part 2. − Electrochemically Grown Hydrous Iridium Oxide. *JEAC* **2016**, *774*, 102−110.

(53) Comninellis, C. H.; Vercesi, G. P. Characterization of DSA-Type Oxygen Evolving Electrodes : Choice of a Coating. *J. Appl. Electrochem.* **1991**, *21*, 335−345.

(54) Kotz, R.; Stucki, S.; Scherson, D.; Kolb, D. M. In-Situ Identification of RuO4 as the Corrosion Product during Oxygen Evolution on Ruthenium in Acid Media. *J. Electroanal. Chem. Interfacial Electrochem.* **1984**, *172*, 211−219.

(55) Yun, J.-Y.; Park, M.-Y.; Rhee, S.-W. Comparison of Tetrakis (Dimethylamido) Titanium and Tetrakis (Diethylamido) Titanium as Precursors for Metallorganic Chemical Vapor Deposition of Titanium Nitride. *J. Electrochem. Soc.* **1999**, *146* (5), 1804−1808.

(56) Finke, C. E.; Omelchenko, S. T.; Jasper, J. T.; Lichterman, M. F.; Read, C. G.; Lewis, N. S.; Hoffman, M. R. Enhancing the activity of oxygen-evolution and chlorine-evolution electrocatalysts by atomic layer deposition of TiO_2. *Energy Environ. Sci.* **2018**, DOI: 10.1039/c8ee02351d.